Applied Catalysis B: Environmental 182 (2016) 326–335

Contents lists available at ScienceDirect

Applied Catalysis B: Environmental

journal homepage: www.elsevier.com/locate/apcatb

Ionic liquid-induced synthesis of a graphene intercalated ferrocene nanocatalyst and its environmental application

Sanjiv Sonkaria[a], Hyung-Tae Kim[b], Sung-Yong Kim[a], Nitee Kumari[c], Young Gyu Kim[b], Varsha Khare[c,*], Sung-Hoon Ahn[a,c,**]

[a] Department of Mechanical and Aerospace Engineering, Seoul National University, Daehak-dong, Gwanak-gu, Seoul 151-742, Republic of Korea
[b] School of Chemical and Biological Engineering, Seoul National University, Daehak-dong, Gwanak-gu, Seoul 151-742, Republic of Korea
[c] Institute of Advanced Machinery and Design, Seoul National University, Daehak-dong, Gwanak-gu, Seoul 151-742, Republic of Korea

ARTICLE INFO

Article history:
Received 6 June 2015
Received in revised form 7 August 2015
Accepted 4 September 2015
Available online 14 September 2015

Keywords:
Ferrocene
Ionic liquid
Reduced graphene oxide
Hexavalent Cr
Redox activity

ABSTRACT

Redox active processes between the π-conjugated system of ferrocene and graphitic surfaces of oxidized or reduced graphene oxide represent a growing area of interest for the development of tunable nanocatalytic systems. In this work, anchoring of intercalated cationic and anionic IL components that engage in both covalent and non-covalent interactions and the subsequent reorganization of IL–rGO bonds after ionothermal decomposition and water hydrolysis of reactive complexes suggests that IL functionalized rGO leads to a regional rearrangement of the carbon–carbon atomic network. The results of this study emphasize the combined solvent and templating properties of [BMIM][$FeCl_4$] at the rGO–IL interface that synthetically directs the self-assembly of a non-hexagonal organometallic structural framework composed of nano-regimes of Fe(II) cyclopentadienyl ring complexes in a reduced graphene oxide matrix. The results show that the atomic rearrangement is consistent with the structural and behavioral characteristics of ferrocene. The capability of rGO-IL and its potential use as an environmental nanocatalyst was demonstrated by its ability to reversibly switch redox states between Fe(II) and Fe(III) corresponding to the ferrocene–ferrocenium redox pair permitting electron transfer from Fe to toxic Cr(VI) and its subsequent reduction to a non-toxic organometallic. A more general conclusion shows that the architectural geometry of the resulting solvated structure formed from the hybridization of ILs and rGO can be used to generate structurally driven properties that further diversify or impart new functionalities to graphitic structures by controlled synthesis from core materials. To the best of our knowledge, this is the first demonstration of a synthetic based approach for the assembly of ferrocene using the structure directing properties of ionic liquids and this route increases the scope of exploiting the electro-redox chemistry and potentially useful magnetic properties of ferrocene functionalized graphene hybrid materials for broader applications.

1. Introduction

An appreciation of the challenges in implementing new nano based technologies has led to an increasing focus on methods to control material properties and the physicochemical factors influencing material characteristics at the nanoscale. This singular aspect of nanomaterials engineering has motivated researchers to explore the growing potential of fabricating hybrid material compositions to address the balance between applicability and controllability. The chemical assembly of nanostructures that acquire catalytic function through surface modification or functionalization as hybrid materials including redox metal nanocatalysts [1] are demonstrably important tunable materials of broad applicability for environmental applications. The development of catalysts with improved efficiencies has also re-directed efforts to engineer products of a 'green' nature to curtail the effects of environmental pollution without comprising performance. The hazardous nature of modern day water pollutants [2] including the biological effects of heavy metals has undoubtedly become an increasingly important consideration in the design and practical application of 'greener' [3] nanocatalysts for the containment and removal of harmful contaminants.

* Corresponding author.
** Corresponding author at: Department of Mechanical and Aerospace Engineering, Seoul National University, Daehak-dong, Gwanak-gu, Seoul 151-742, Republic of Korea.
E-mail addresses: khare@snu.ac.kr, vkharein@gmail.com (V. Khare), ahnsh@snu.ac.kr (S.-H. Ahn).

http://dx.doi.org/10.1016/j.apcatb.2015.09.008
0926-3373/

An important focus in the elemental design of 'greener' and superior nanocatalysts has increasingly concerned the development of heterogeneous catalytic systems. This rationalization has further led investigators in search of naturally occurring abundant materials as effective alternatives to replace more expensive metallic catalytic components which are also economically disadvantaged by issues associated with their recovery [4] and relative low occurrence. However, the interaction of noble metals with graphene have been pursued with much interest [5]. Notably, the complexation of iron is an outstanding example of a cost-effective material that exhibits chemical and redox properties allowing its integration with carbon supported nanomaterial surfaces for catalytic functions. An example is the degradation of organic pollutants by iron doped graphene oxide (Fe–GO) *via* UV light activation of hydrogen peroxide suggesting a significant role for iron mediated metal catalysis [6] by exploiting the redox characteristics of the metal. This may be further enhanced by the tunable electronic properties of the graphene environment. It is plausible therefore to rationalize that the extent of electron donor and acceptor events in transition metal complexes of graphene might be governed by the structure of the metal complex and atomic arrangement within graphene. This may be a strongly influencing factor of catalytic efficiency.

In recent years, a growing number of studies reporting the nano-hybridization of ferrocene (F_c) [$(C_2H_5)_2Fe$] organometallic iron complexes with graphene have emerged in which covalently [6–8] and non-covalently [9] immobilized ferrocene and modified ferrocene [10] have been introduced to prepare iron based graphene supported metallocenes for a number of applications. Ferrocene and their derivatives have shown exceptional selectivity towards divalent metals [11] demonstrating their potential for heavy metal detection and catalytic removal facilitated by the 6d electron arrangement of Fe(II) complexed between π electron donating cyclopentadienyl ring structures. Hence, the utilization of ferrocene groups towards the degradation of harmful chemical pollutants *via* oxidation or reduction processes are potentially effective routes to neutralize their toxic effects through the formation of stable non-toxic products. The photo-induced charge transfer activity between graphene oxide (GO) and ferrocene in ferrocene modified GO sheets was recently demonstrated [12] showing that the photo-exciton state of graphene is highly responsive to the redox properties of ferrocene when anchored to the GO surface. This finding signified the potential application of ferrocene to function as a nanocatalytic reducing agent [13] for the detoxification of metals when stabilized within the graphene–ferrocene complex. Considering that the synthesis of ferrocene prepared by the reaction of cyclopentadienyl anions $(C_2H_5)_2$ and ferrous cations (Fe^{2+}) is potentially hazardous because of the cautionary nature of the starting materials, we explored the possibility of using another approach. In the interest of pursuing an environmentally friendly method for the application of ferrocene selectivity as a catalyst for the reduction heavy metals, the use of a single multi-component green material to direct the synthetic assembly and support the catalytic properties of ferrocene is highly desirable.

The fabrication of graphene and ionic liquid (IL) hybrid compositions provide unique opportunities to combine the characteristics of high surface area materials with multi-functional agents that may operate simultaneously as stabilizers, surfactants, polar solvents, catalysts and as powerful structural templates from the combined effect of the cationic and anionic components. One rationalization for the current work is based on the reported observation that imidiazolium ILs can be applied for the synthesis of metallocene structured ionic ligands for biphasic reactions [14] and show remarkable ability to influence favourable electronic properties as demonstrated by the synthesis of a cationic cobaltocenium in 1-butyl-3-methylimidazolium hexaflurophosphate [BMIM]PF_6] [15]. This approach is strengthened from the reported observation that imidazolium IL-transition metal salts can be applied for the synthesis of ring structured carbon based precursors such as graphene [16]. We extended this hypothesis for the first time by pursuing the self-assembly of an intercalated ferrocene reduced graphene oxide nanocomposite *in situ* using a one pot synthesis approach. The IL properties of bis(1-butyl-3-methylimidazolium) iron(II) tetrachloride [BMIM][$FeCl_4$] was investigated at the graphene/IL solid–liquid interface in the presence of glycerol to examine if the functional nature of the reduced graphene oxide (rGO) surface was sufficiently compatible to support an alternative route for a readily assembled rGO–FeIL catalyst.

Here, we demonstrate an alternative 'green' approach to the conventional methods of introducing ferrocene or ferrocenyl moieties at the reduced graphene oxide (rGO) interface different to the widely reported processes using covalent or non-covalent grafting of ferrocene at the graphitic surface. In an ionothermal assisted process, the intercalation of synthetically derived ferrocenyl moieties was achieved by exploiting the self-assembly properties of [BMIM][$FeCl_4$] with GO under reducing conditions *via* a defect-rich rGO mesoporous structure. Defects stabilized to form a self-assembled cyclopentadienyl ring configuration consistent with the structural characteristics of ferrocene/ferrocenyl moieties through the intercalation of Fe from the interaction of rGO with $[FeCl_4]^-$. We conclude that the role of the cationic $[BMIM]^+$ in ordering the orientation of the geometrical interplaner spacing between graphitic sheets through non covalent interactions was a key event in permitting complexation of $[FeCl_4]^-$ at the rGO interface. Stabilized catalytic centers on a reduced graphene oxide (rGO) support provides for an organometallic framework that facilitates the transfer of electrons *via* a reversible ferrocene–ferrocenium redox center in a host-guest dependent manner. This was demonstrated by the effective reduction of toxic chromium(VI) to its non-toxic Cr(0) oxidation state retained by the rGO matrix. Extensive structural and spectroscopic analysis showed for the first time that a synthetic based approach was highly effective in driving the self-assembly of a rGO-FeIL ferrocene/ferrocenium redox catalyst with the ability to efficiently reduce milligram quantities of hexavalent chromium.

2. Experimental

2.1. Synthesis of Fe-IL

The iron(II) based IL was prepared according to a similar procedure as described in the previous report. Anhydrous iron(II) chloride ($FeCl_2$), 1-methylimidazole and butyl chloride were purchased from Alfa-Aesar. 1-Methylimidazole and butyl chloride were purified by distillation. Anhydrous $FeCl_2$ was used without further purification. To a stirred solution of 1-methylimidazole (100.0 mmol, 8.21 g) in acetonitrile (80 mL), butyl chloride (120.0 mmol, 11.1 g) was added drop wise at 0 °C. The reaction mixture was stirred for 24 h at 80 °C. Removal of the solvent under reduced pressure afforded 1-butyl-3-methylimidazolium chloride (Bmim-Cl) as a white solid. The crude product was purified by washing with diethyl ether and ethyl acetate, respectively. Completion of the reaction was confirmed by ^{1}H NMR spectra. The ^{1}H NMR spectra were obtained using $CdCl_3$ as solvent on a JEOL JNM LA-300 spectrometer (300 MHz for ^{1}H NMR). The ^{1}H NMR data were reported as follows in ppm (δ) from the internal standard (TMS, 0.0 ppm), chemical shift (multiplicity, coupling constant in Hz, integration). 1-Butyl-3-methylimidazolium chloride (Bmim-Cl): Yield 15.4 g (89%); ^{1}H NMR δ 0.95–1.00 (t, J = 7.2, 3H), 1.34–1.46 (m, 2H), 1.86–1.99 (m, 2H), 4.14 (s, 3H), 4.87 (t, J = 7.2 2H), 7.3 (s, ^{1}H), 7.45 (s, 1H), 10.87 (s, ^{1}H). Bmim-Cl (80 mmol, 14.0 g) and anhydrous $FeCl_2$ (40 mmol, 5.07 g) were mixed in a glove box and the mixture was

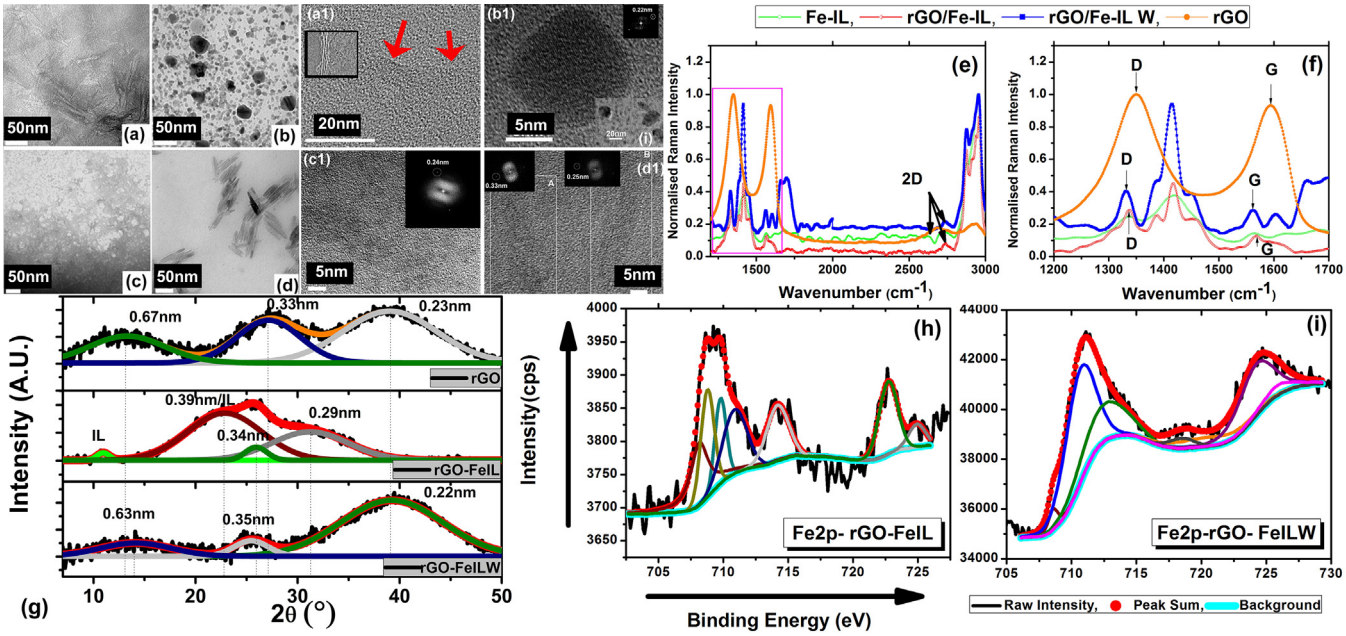

Fig.1. Structural and microstructural properties of Fe-IL, rGO/Fe-IL, rGO/Fe-ILW and rGO. (For interpretation of the references to colour in this figure legend, the reader is referred to the web version of this article.)
Transmission electron micrographs of (a) rGO showing the presence of typical wrinkled sheets (b) rGO-FeIL nanohybrid exhibiting nanodiscs of rGO filled with IL (c) rGO-FeILW water washed nanohybrid indicating the presence of mesoporous structure of nanohybrid (d) supernatant of rGO-FeILW with the nano needles of graphene. HRTEM images show (a1) rGO characterized by wrinkled morphologies composed of single graphene layers (indicated by red arrows) with few layer sheets in local regions shown in the inset of Fig. 1 (a1) and (b1), An enlargement of the nano discs is shown in inset (i) together with the FFT (top right corner of image b1) (c1) rGO-FeILW mesoporous structure indicating the presence of rGO with some lattice expansion of 0.24 nm determined from the FFT (top right corner of image c1) (d1) calculated interlayer spacing of 0.25 and 0.31 nm from the FFT of image d1 shown in the inset of d1 (e) comparative Raman spectrum of FeIL, rGO-FeIL, rGO-FeILW and rGO (f) enlargement of the bordered region in (e) showing the shift of D and G peaks in hybrid materials (g) comparative de-convoluted WAXS pattern of rGO, rGO-FeIL and rGO-FeILW indicating the presence of FeOCl in rGO-FeIL and the multidirectional increase in interlayer spacing in rGO-FeILW (h) comparative deconvoluted Fe2p core level spectra for FeIL and rGO/Fe-ILW with two spin-orbit doublets (Table S3). Shirley background scheme was used for the fitting of the spectra (For interpretation of the references to colour in this figure legend, the reader is referred to the web version of this article).
Further, HRTEM imaging of rGO in Fig a1 show the existence of single layer reduced graphene oxide (indicated by red arrows) with few layer sheets in local regions as shown in the inset of Fig. 1. (a1). Fig. 1 also shows a detailed HRTEM view of an IL embedded nanodisc representing an enlarged view of a single nano disc shown in inset Fig. 1. (b1). The lattice distance of 0.22 nm derived from the Fast Fourier Transform (FFT) (top right corner of image b1) is consistent with the presence of rGO and the observed dark contrast signifies an IL rich enviroment. However under a concentrated electron beam, the phase contrast is reduced because of the removal of IL. The expulsion of the IL from the nanodisc does not alter the lattice fringes strongly indicating that rGO is a stable component of the system.

heated to 140 °C and stirred under argon atmosphere. After stirring for 24 h, the mixture was cooled to room temperature. Bis(1-butyl-3-methylimidazolium) iron(II) tetrachloride was obtained as a brown liquid. Bis(1-butyl-3-methylimidazolium) iron(II) tetrachloride: yield 19.1 g (>99%); Anal Calcd (%) for $C_{16}H_{30}N_4Cl_4Fe$: C, 40.4; H, 6.35; N, 11.8. Found: C, 39.7; H, 6.37; N, 11.5.

2.2. Synthesis of nanohybrid materials

Nanohybrids of rGO and Fe containing IL (rGO-FeIL) were synthesized by a one-pot reduction method reported previously by Khare et al. [17]. Graphene oxide dispersed in water was dried at 100 °C for 24 h period resulting in a dispersion of Fe containing IL with the chemical formula ([BMIM][$FeCl_4$]). The preparations were subjected to ultra-sonication for 30 min at room temperature to assist further mixing of Fe-IL and GO followed by the addition of glycerol to the graphene oxide FeIL suspension to reduce GO to rGO at 90 °C for 24 h.

2.3. Cr(VI) sorption test using simulated water

The investigations of heavy metal sorption of pollutants from simulated waste water were conducted using hexavalent chromium obtained by extraction from potassium dichromate solution at a stock concentration of 25 mg L^{-1}. The simulated water was treated with pure rGO and rGO–FeIL and rGO–FeIL was subjected to a repeated wash cycle of five rounds to obtain rGO–FeILW. The simulated water was mixed overnight with known concentrations of rGO, rGO–Fe-IL and rGO–FeILW (8.0 mg L^{-1}) by agitation in a shaker and finally the solutions were centrifuged to separate the supernatant for ICP-MS analysis. Further after sorption, sediments composed of rGO–IL and rGO–ILW and the respective supernatant fractions designated rGO-IL1 and rGO–ILW1 were investigated by WAXS, XPS and HRTEM.

2.4. Characterizations

Wide-angle X-ray scattering (WAXS) was performed using Cu Kα radiation in the 2θ range of −100° to +168°. Transmission electron microscopy (TEM) measurements were conducted on Carl Zeiss energy filtered TEM (EF-TEM), LIBRA 120 operated at 120 kV. High resolution TEM (HRTEM) was performed on JEM03013 (JeOL) with a resolution of 0.14 nm for lattice imaging and 0.17 nm for point imaging. The Raman spectra were recorded by a RenishawVia Raman microscopy equipped with a 514 nm Ar laser. All measurements were performed at room temperature. X-ray photoelectron spectroscopy (XPS) was conducted using a Kratos AXIS-Hsi spectrometer with a monochromatic Mg-Kα X-ray source, with a multi discrete detector. After recording the XPS spectrum, accurate binding energies (±0.1 eV) were determined with respect to the position of adventitious carbon at 284.5 eV for compensating sample charging effect. The reference C1s binding energy was calculated by measuring the XPS of graphite powder as a standard.

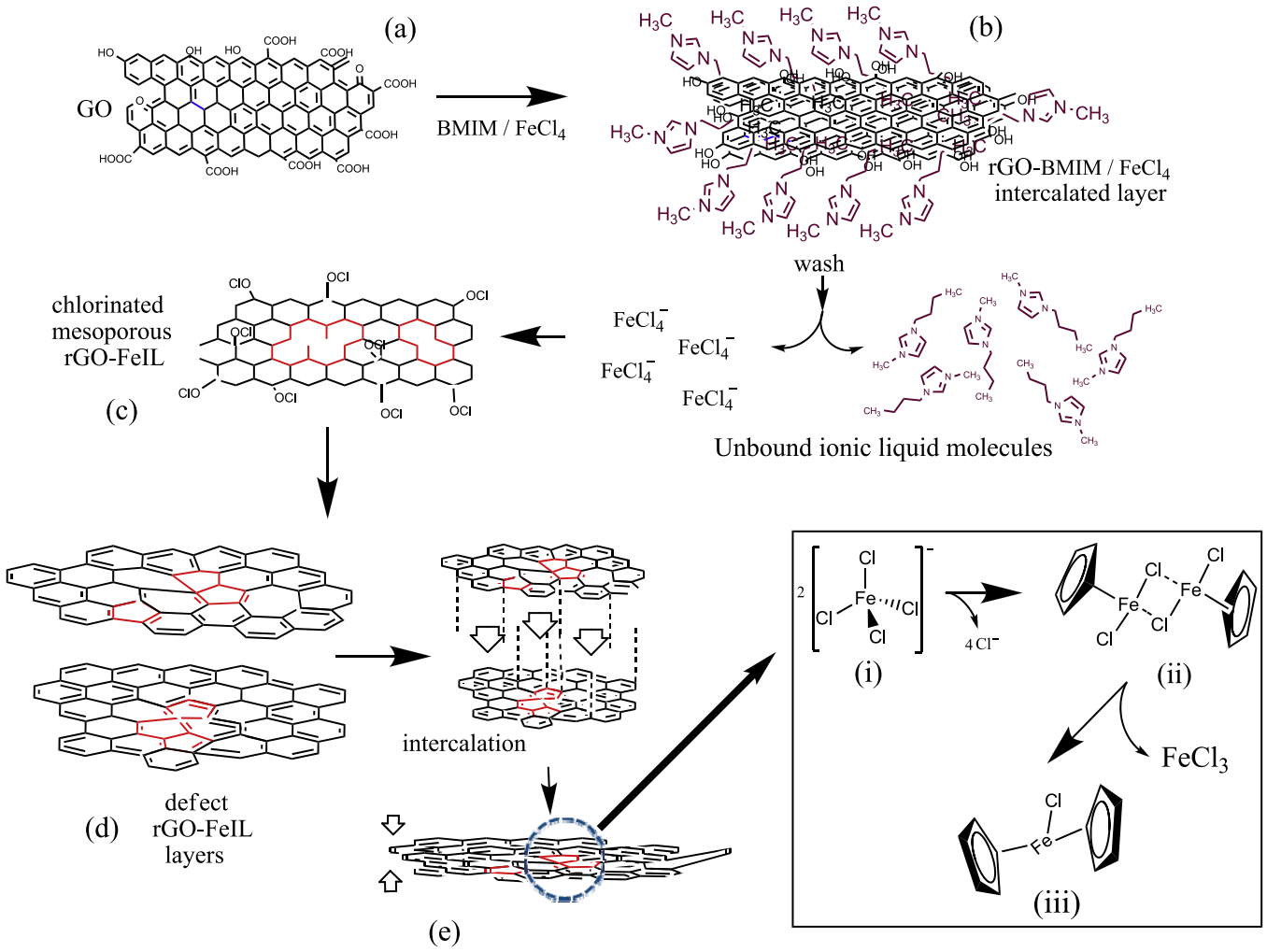

Scheme 1. Chemical events between rGO and FeIL leading to the intercalation of Fe at defect positions (shown in red) stabilized by a ferrocene/ferrocenyl configuration. (For interpretation of the references to colour in this figure legend, the reader is referred to the web version of this article.)
(a) The reduction of GO in glycerol in the presence of [BMIM][$FeCl_4$] results in the formation of (b) functionalized rGO-BMIM $FeCl_4$ with BMIM cationic alkyl chain localized in the interlayer spacing of rGO. Removal of IL embedded in rGO by washing of the hybrid material generates an (c) intermediate mesoporous rGO structure in a chlorine anionic enviroment with increased structural defects. The intercalation of Fe occurs through (d) the stabilization of ferrocene/ferrocenyl self-assembly process between interlayers of rGO that may occur *via* an (e) unstable chlorine bridged cyclopentadienyl dimer in an Fe assisted process.

3. Results and disccusion

The templating properties of the imidiazolium structured IL [BMIM][$FeCl_4$] or Fe-IL on the graphitic matrix was initiated by mechanical agitation and sonication to generate a homogeneous phase after water dispersion of GO under heat. To explore the ionothermal [18] effects of the IL as a metal precursor and the extent of its participation as an active reactant in modifying the structural framework of rGO in addition to its solvent and templating properties, the self-assembly of rGO–FeIL at the solid–liquid interface was investigated under mild reducing conditions. Although the controllability and scalability of rGO are two important parameters supporting its use as a modifiable material, structural deviation from the pristine graphene architecture to its reduced form accommodating defect geometries is generally viewed as undesirable [19]. Low contrast wrinkled sheet morphologies of rGO in the absence of IL is consistent with the presence of a few layers of rGO (Fig. 1a) as evidenced by TEM and intrinsically reflects mechanical deformations to regain thermodynamic stability arising from loss of ordered oxygen bonds. Further, HRTEM imaging of rGO in Fig. 1(a1) show the existence of reduced graphene as single layered sheets. This reduced state is further supported by the absence of the (002) signature peak characteristic of GO at 11.7° in the WAXS pattern of rGO shown in Fig. 1(g). A drastically reduced carbon–oxygen ratio in rGO observed here highlights the effective reducing properties of glycerol [20] as a viable 'green' alternative [21] to more conventional agents such as sodium hydrogen tetraborate. Interest in the role of glycerol as a reductant further relates to its superior solvent properties suited to hydrophobic materials particularly under ionothermal conditions [22], its ability to function in metal catalyzed hydrogenation of unsaturated nitrogen and carbon organic groups and dispersing transition metal complexes favoring the assembly of metal-nanoparticle complexes [23]. We rationalized the possibility of exploiting these characteristics within the framework of the metal rich [BMIM][$FeCl_4$] IL as a reaction medium to increase the scope of Fe intercalation in the rGO lattice. In the 'wrinkled' state, topological folding of the graphene membrane and the occurrence of layered orientations formed by regions of high curvature and flat planes imply the presence of higher order ring configurations conforming to either hexagonal, non-hexagonal or indeed an alliance of ring symmetries forming nanoregimes of *n*-polygon networks. This phenomena is commonly observed by a Raman shift in the I_D/I_G ratio of rGO (Fig. 1e and f) (parameters summarized in Table S1). The reduced oxygen

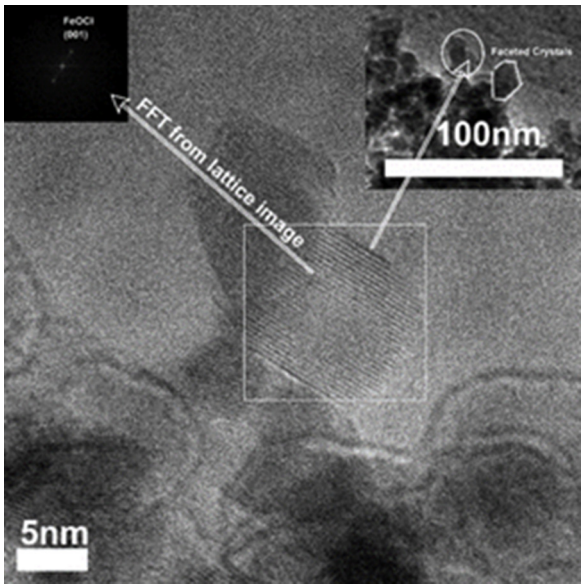

Fig. 2. HRTEM imaging and FFT analysis of a well faceted rGO-embedded iron oxychloride crystal.
Fast fourier transform analysis (inset; upper left hand side) of lattice fringes of the bordered region showing the occurrence of a faceted crystal of FeOCl (001 plane) embedded in the rGO lattice.

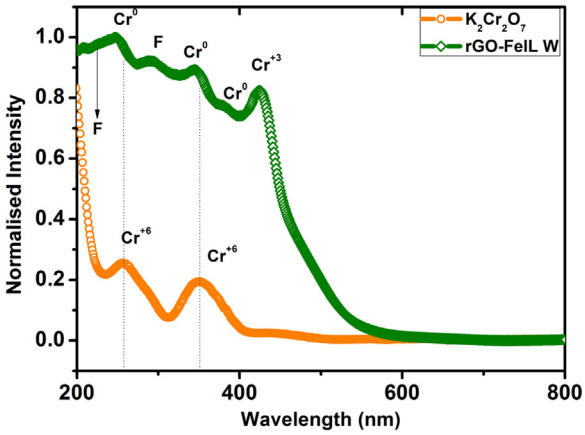

Fig. 3. UV–vis spectra of rGO-FeILW before and after exposure to chromium.
The UV–vis spectra corresponds to the sorption bands for the reduction of Cr^{6+} to Cr^{3+} and Cr^0 and bands corresponding to the existence of ferrocene/ferrocenyl moieties. The broadening of the bands that occur at higher wavelengths also signify the reduction of higher Cr oxidation states to Cr^0.

content in the presence of glycerol as a largely unexplored reductant in graphitic systems, necessarily accompanies an increase in the hydroxyl group functionality leading to its participation as a donor and acceptor of hydrogen bonds. It has been reported that hydrogen bonding events of hydroxyl groups are critical to the folding process [24] and the surface energetics of cavity like morphologies of constrained folds in their tendency to reduce bond orientations to lower energy ringed configurations might be relieved through their associations with ILs.

This prediction is observed by the dominant ionic character of [BMIM][$FeCl_4$] IL which exerts shape changing properties to rGO from wrinkled sheets to nanodisc type rGO-FeIL morphologies of 5–50 nm (Fig. 1b) by *in-situ* reduction similar to a previous study in the presence of IL [20]. The substantially altered morphological state of rGO in the IL reaction medium is indicative of a high degree of interaction at the rGO–IL interface revealing the structural dependence of rGO on the cationic/anionic environment. Fig. 1(b1) shows a detailed HRTEM view of an IL embedded nanodisc representing an enlarged view of single nanodiscs shown in inset Fig. 1(i). The lattice distance of 0.22 nm derived from the Fast Fourier Transform (FFT) (top right corner of image in Fig. 1(b1) is consistent with the presence of rGO and the observed dark contrast signifies an IL rich enviroment. Increase in the interlaying spacing of rGO–FeIL by 8–11% relative to rGO from the deconvoluted WAXS pattern (Fig. 1g) (parameters shown in Table S2) was strongly suggestive of the presence of intercalated layers of Fe-IL within the graphitic structure implying the establishment of a commonly observed cationic/anionic layering effect occupying a large surface area [25]. The structural ordering or templating properties of the IL solvent materializes during the washing phase of rGO–FeIL revealing the depth of the inter-ionic interactions and molecular forces governing morphological changes to the functionalized graphitic lattice. Exposure of water to rGO–FeIL resulted in partial destabilization of the hybrid structure to form rGO–FeILW (five repeated washing steps) of mesoporous character (Fig 1c) generated from the removal of nanodiscs from the graphene sheets. The interlayer spacing of rGO occupied by FeIL ions also diminished accompanied by an increase in sp^3 bonding (0 0 1) in the direction of h 0 0 after hydrolysis suggesting the release of trapped IL from the mesoporous structure. The increase in bonding layers of mesoporous rGO–FeILW was supported by HRTEM imaging in Fig. 1 (c1) indicating the presence of rGO with a lattice expansion of 0.24 nm as derived from the FFT (top right corner of image Fig. 1(c1)). The probable event that explains this observation may be consistent with the disruption of the π–π stacking of the imidazole group of the IL intercalated between graphene layers which is often associated with aromatic groups [26]. We have also performed TEM on intermediate stages of washing to show the effect of partial removal of the IL. Fig S1 represents TEM imaging of rGO layers obtained after one washing cycle. We note that the presence of water initiates the simultaneous occurrence of nanodiscs shown in inset (b) which is representative of an enlarged view of the bordered region shown in the bold circle and the formation of needles resulting from folding of nanoregions of the IL functionalized rGO sheets (Fig S1; inset b and c). Further, initialization of these structures is clearly visible all along the length of the sheet. HRTEM analysis of the encircled regions reveal lattice fringes of different interplaner spacing clearly visible in the FFT in the range of 0.21–0.70 nm. The water expelled nanodiscs unsupported by the IL environment collapsed to form needles that were proportionately similar in length to the diameter of the pore size created from their removal (Fig. 1d). Compositionally, energy dispersive spectroscopy (EDS) analysis shows that needles are abundantly composed of carbon (wt%: 93%) and the contribution of Fe is very low (wt%: 1.4%) (Fig S2). This signifies that the surrounding environment of the needles may be relatively lower in IL. The needle like morphologies exhibited interlayer spacing typically of the order of 0.25 and 0.31 nm exemplified by HRTEM analysis of regions A and B shown in Fig. 1 (d1). The analysis of water washed rGO–FeILW mesoporous samples signified a proportionally higher number of defect sites as vacant regions after washing. Notably, the largest blue shift in the I_D/I_G ratio correlated to rGO–FeILW compared to both rGO and rGO–FeIL (Fig. 1e and f) suggesting that the origin of the newly formed defect sites were formed by water displacement in the mesoporous structure. This is shown by the expansion of the bordered region of the Raman peaks in Fig. 1e shown in Fig. 1f and this interpretation agreed well with the TEM imaging.

Application of sum frequency generation (SFG) vibrational spectroscopy has shown that binding of the CH_2- backbone of the butyl alkyl chain of BMIM is orientated parallel to the graphitic surface while the BMIM ring is only weakly associated with graphene lattice *via* the methyl group moiety [27]. In contrast, the anionic methyl sulfonate $[SO_3CH_3]^-$ IL component in the above study resembling the tetrahedral geometry of the high-spin d^5 iron of

the tetrachloroferate $FeCl_4^-$ complex of [BMIM][$FeCl_4$] caters for a stronger SFG resonance signal that originates from the stronger bonding interaction of hydrogen in $\cdots H\cdots O\cdots S(=O)_2CH_3$ with the electron dense graphene surface stabilized by the conjugate base $^{=}O-S(=O)_2CH_3$. The probable weak associations of BMIM with rGO akin to π–π stacking and/or van der waal forces is sufficient to permit the expulsion of layered cationic imidazole rings observed here decreasing the interlayer spacing of rGO. However, the interlayer carbon–carbon spacing of rGO–FeILW in the range of 0.23–0.63 nm (Table S2) is considerably above the average stacking distance of covalently bonded graphene sheets around 0.156 nm [28]. The partial collapse of dispersed rGO layers implies a key role for $FeCl_4^-$ in maintaining a good degree of dispersity of rGO in the absence of the IL solvent replaced predominately by water. Based on these findings, here we infer the potential role of metals or metal complexes and their ability to prevent self-aggregation of sheets by acting as spacers [29]. This could also serve as a general route to minimize the loss of surface area by intercalation. However, the thermodynamic barrier to this realization necessarily demands a high energy contribution for the destabilization of the graphene honey comb structure to permit the covalent intercalation of Fe resulting in Fe-C bond formation. To decrease the energy burden at vacancy sites in rGO however, suggests that the deformation of existing defect sites under favourable conditions may play a key role in the re-structuring of rGO to accommodate $FeCl_4^-$.

To explore the feasibility of a metal intercalated rGO assembly from the chemical interaction with Fe-IL, we compared the Fe2p core level spectra of ionothermal products rGO–FeIL (before water hydrolysis) and rGO–FeILW (after water hydrolysis). The assignment of XPS peaks showed signals at 708.84 eV for rGO–FeIL and 719.87 eV for rGO–FeILW (Fig. 1h and Table S3) corresponding to the binding energies of ferrocenyl moieties respectively (Fe in the +2 oxidation state) as observed elsewhere [6,30,31]. The generation of an organometallic framework through the intercalation of Fe is likely aided by the presence of defect intensities identified and constitutes around 36–40% in both rGO–FeIL and rGO–FeILW. In an energy driven process, the flexible integrity of graphitic materials predicted by density-functional theory (DFT)

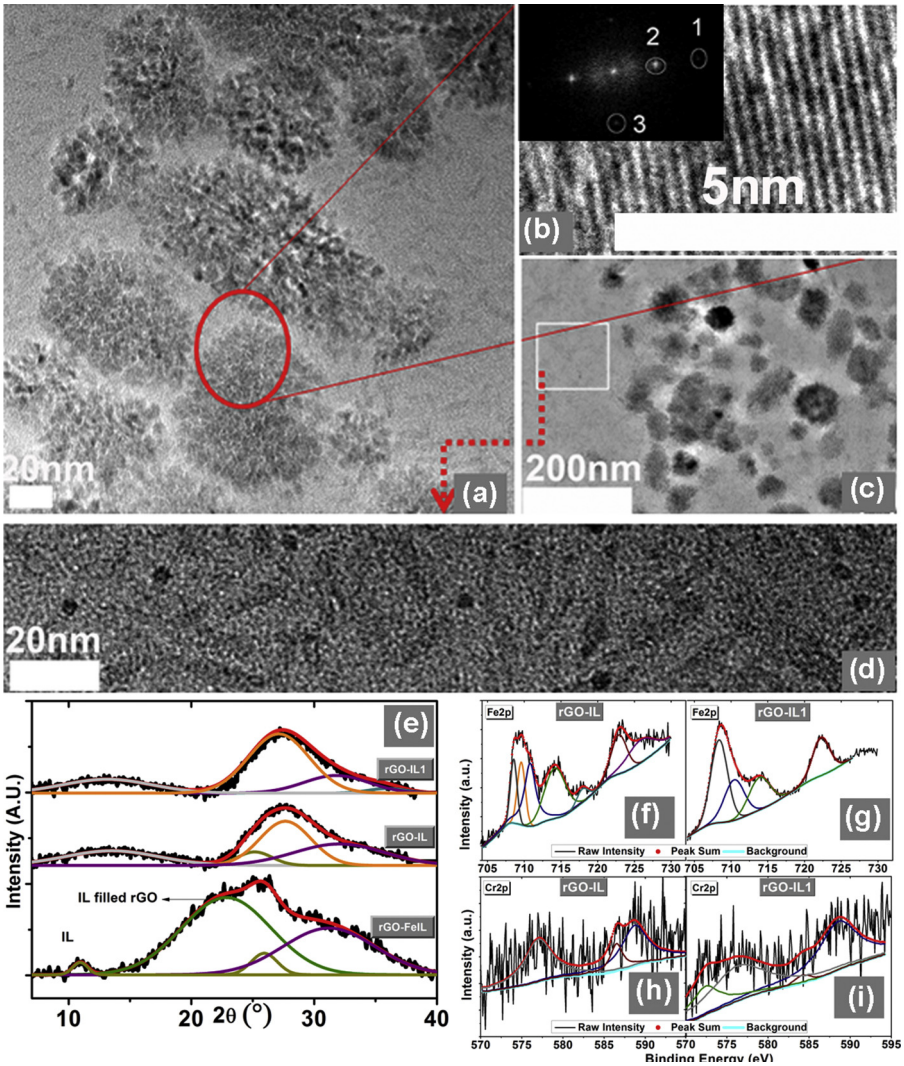

Fig. 4. Morphological and surface characterization of rGO-IL (sediment) and rGO-IL1 (supernatant) after chromium sorption. (For interpretation of the references to colour in this figure legend, the reader is referred to the web version of this article.)
HRTEM images of rGO-IL nano hybrid after chromium sorption showing (a) floral mushroom like arrangement of nanostructures, (b) lattice image of the mushrooms bordered within red circle, (c) magnification of the mushroom region suggesting the genesis of mushrooms as a hydrogen bonded porous network of nanodiscs and (d) magnified image of the squared region showing the presence of weakly contrasting needles and individual nanodiscs (f) Fe2p core level spectra of the sediment and supernatant of rGO-IL-1 and (g) rGO-ILW hybrid materials after hexavalent Cr sorption (h) A comparative deconvoluted Cr2p core level spectra of rGO-IL with binding energies characteristic of Cr^{3+} (59%) and largely complexed as $CrCl_3$ and (i) rGO-IL1 also complexed mainly in the Cr^{3+} oxidation state (60%) as Cr_2O_3 (For interpretation of the references to colour in this figure legend, the reader is referred to the web version of this article.).

calculations supported by experimental imaging by TEM reports the existence of localized non-hexagonal geometries within the sheet structure that originates from random loss of carbon from the graphene lattice [32]. Such structural defect configurations composed of essentially 'missing' or 'displaced' atoms are characterized by their susceptibility to regain energetically favored arrangements by carbon substitution with metals [33] leading to pentagonal geometries as one possible arrangement that further acquires thermodynamic stability by intercalating Fe or Fe complexes forming ferrocene of ferrocenyl moieties.

In our efforts to understand the synthetic assembly process of rGO-ferrocene hybridization based on the experimental observations, chemical and structural characteristics of [BMIM][$FeCl_4$] at the graphene interface and the consistency of these interpretations with reported works, we rationalize a possible route identifying some key events. The tetrachloroferrate $FeCl_4^-$ ion exhibits an asymmetric tetrahedral geometry but also the structure presents an inverted bonding configuration that places Fe(3d) orbitals below Cl(3p) [34] decreasing the degree of metal-ligand covalency and the Fe—Cl bonds substantially weaken due to a change in the phase transition between 300 to 450 K [35]. In view of the preferential binding of metals at defect sites resulting in the stabilization of dangling bond energies through the formation of C—M (carbon-metal) associations by establishing ring closure [36] and the active role of Fe in assisting this process [37], the high metallic character and relative stability of $FeCl_4^-$ suggests a complexation step of $FeCl_4^-$ with an unoccupied defect carbon of rGO. Weakening of the Fe—Cl bond [35] followed by the partial release of Cl^- ions from the $FeCl_4^-$ complex is evidenced by analysis of Cl2p core level spectra environment in Fe-IL (Fig. S3) resulting in the occurrence of free ionic Cl^- with a binding energy of 196.8 eV. The availability of free Cl^- is further evidenced by spin orbit splitting of the Cl2p peak of FeIL resulting in another doublet (ΔBE = 1.7 eV) corresponding to $FeCl_4^-$(199.9 eV) and a low C–Cl peak intensity at 201.6 eV accompanied by a much more pronounced peak intensity split of 200.3 and 201.9 eV suggesting widespread chlorination of the rGO surface. These events might be consistent with the formation of an unstable chlorine bridged dimer of cyclopentadienyl iron dichloride which further destabilizes to form a chlorinated ferrocenyl moiety [38] shown in Scheme 1. This is different to the stable cyclopentadienyl iron dicarbonyl dimer organometallic [39] arrangement in which the central Fe contributes two, one, or zero electrons [40].

The scenario in Scheme 1 is further supported by the liberation of Fe from the dissociation of Fe—Cl and the subsequent occurrence of iron oxide variants FeO (27.3%) and $FeCl_3$ (14.3%), from analysis of the Fe2p spectra with associated binding energies 709.85/722.78, 710.93 and 714.24 respectively (Table S3). The variable oxidation states of simple Fe complexes might arise from the possible interaction with water and the presence of hydroxyl and epoxy groups on the surface of reduced graphene oxide as deduced from the C1s and Cl2p (Fig. S3) core level spectra. Also noted was the generation of the metastable iron oxychloride (FeOCl) evidenced by Fe2p doublet peak area in rGO–FeIL (16.01%) which increased 2.4-fold (54.92%) in rGO–FeILW after water hydrolysis of rGO–FeIL to rGO–FeILW (Table S3). The presence of FeOCl also featured in the WAXS pattern in rGO layers (22.85°) (Fig. 1g and Table S2) highlighting a possible role in the electron charge distribution [41] on the graphitic structure. The IL trapped layers of observed d-spacing 0.81, 0.39 and 0.34 nm is close to the interplaner spacing of (0 1 0), (1 0 0) and (0 0 1) planes of FeOCl. This metastable compound with orthorhombic space group Pmnm with lattice spacing $a = 0.38$, $b = 0.79$ and $c = 0.33$ nm (JCPDS-24-1005) possibly forms by the interaction of Fe_2O_3 and $FeCl_2$ [42–43]. To substantiate and further support the co-existence of rGO-FeILW and the chemically formed iron oxychloride, we explored HRTEM as a tool to provide visual evidence of inorganic crystals. The analysis of the lattice fringes of the bordered region in Fig. 2showed faceted crystal growth (Fig. 2; inset (upper right hand side)) distinct from the graphitic matrix and an associated FFT (Fig. 2; inset (upper left hand side)) pattern consistent with the assembly of FeOCl. The nanocrystals are well faceted in contrast to rGO nanodiscs exhibiting non-faceted circular morphologies as indicated in the inset. The HRTEM of these faceted crystals confirm the presence of 001 planes of FeOCl.

Ferrocene is a strong mediator of electron charge transfer and operates effectively as an electron donor in the presence of a recipient electron acceptor. To explore the electron donating properties of rGO-ferreocene conjugate, the nanocatalytic redox characteristics were investigated using chromium Cr(VI) reduction as our model reaction. As mentioned, the interlayer carbon–carbon spacing of rGO–FeILW in the range of 0.23–0.63 nm (Fig. 1g, Table S2) is considerably above the average stacking distance of covalently bonded graphene sheets around 0.156 nm [28] which might signify the probable inter atomic positioning of ferrocene molecules in rGO-FeIL and the larger separation may be consistent with weakened van der waals force interactions. It is expected that the nanocatalyst composition retains a minimum amount of IL as shown by XPS peaks (Fig. S4) corresponding to residual associations with graphene after washing and therefore does not contribute to the increased interlayer spacing that might exist in π–π stacking.

The stabilization of ferrocene within an organometallic framework such as those of pristine or N-doped graphene surfaces [13] can greatly assist their ability as effective reducing agents. This scenario would be particularly useful for reduction of environmentally toxic metals such as Cr which also behaves as an electrical interconnector when complexed with graphene [44]. Hence, the entrapment of chromium and iron as organometallics can readily participate in electron charge transfer processes modulated by the global nanomaterial environment. A comparison of chromium (VI) removal efficiency of unfunctionlised rGO with Fe-IL functionalized rGO (rGO–FeIL) shows respective removal capacities of 45 and 62% when exposed to a chromium stock of 25 mg L^{-1}.

Since Cr sorption properties of rGO–FeILW is of primary interest here, wherever possible, a brief comparison of the interactions of both FeIL functionalized rGO and unfunctionalized rGO with Cr is discussed to better understand the nature of the nanocatalyst. The analysis showed that ununctionalized rGO showed much lower Cr removal efficiency compared to rGO–FeIL up to 62 and 68% respectively. We monitored changes in the oxidation state of Cr by following the signature pattern of the corresponding UV–vis spectra after a 2 h sorption cycle. A typical UV–vis profile is shown in Fig. 3 and the characteristic peaks at 277 and 351 nm correspond to the O–Cr^{6+} tetrahedral arrangement [45] and results in a complete loss of the observed peaks accompanied by a chemical shift to 425 nm signifying the transition from Cr^{6+} to Cr^{3+}. This change conforms to an octahedral structure assisted by rGO-FeILW sorption enviroment. Band broadening of the spectra can be attributed to the characteristic peak of O–Cr^{3+} at 538 nm with relatively weaker transitions visible in the range of 200–400 nm after sorption. These transitions are close to the reported values for bis-dibenzene chromium [$(C_6H_6)_2Cr$] complex indicated by dotted lines [46,47] and ferrocene/ferrocenyl moieties [30] (shown as F in Fig. 3) [48,49]. The peak and shoulder positions of the centrosymmetric [$Cr(\eta6\text{-}C_6H_6)_2$] 12-carbon coordinated structure are converted into band frequencies and correlated with the reported values (Table S4) [42,43]. The presence of ferrocene/ferrocynal moieties can also be observed by shoulder peaks at sorption bands at 224 and 294 nm (Fig. 3). Further the highest broad band centered at 425 nm was baseline corrected and deconvoluted to observe the presence of $(C_6H_6)_2Cr$ and ferrocene (Fig. S5, Table S5). Evidence of the existence of ferrocene/ferrocenyl type com-

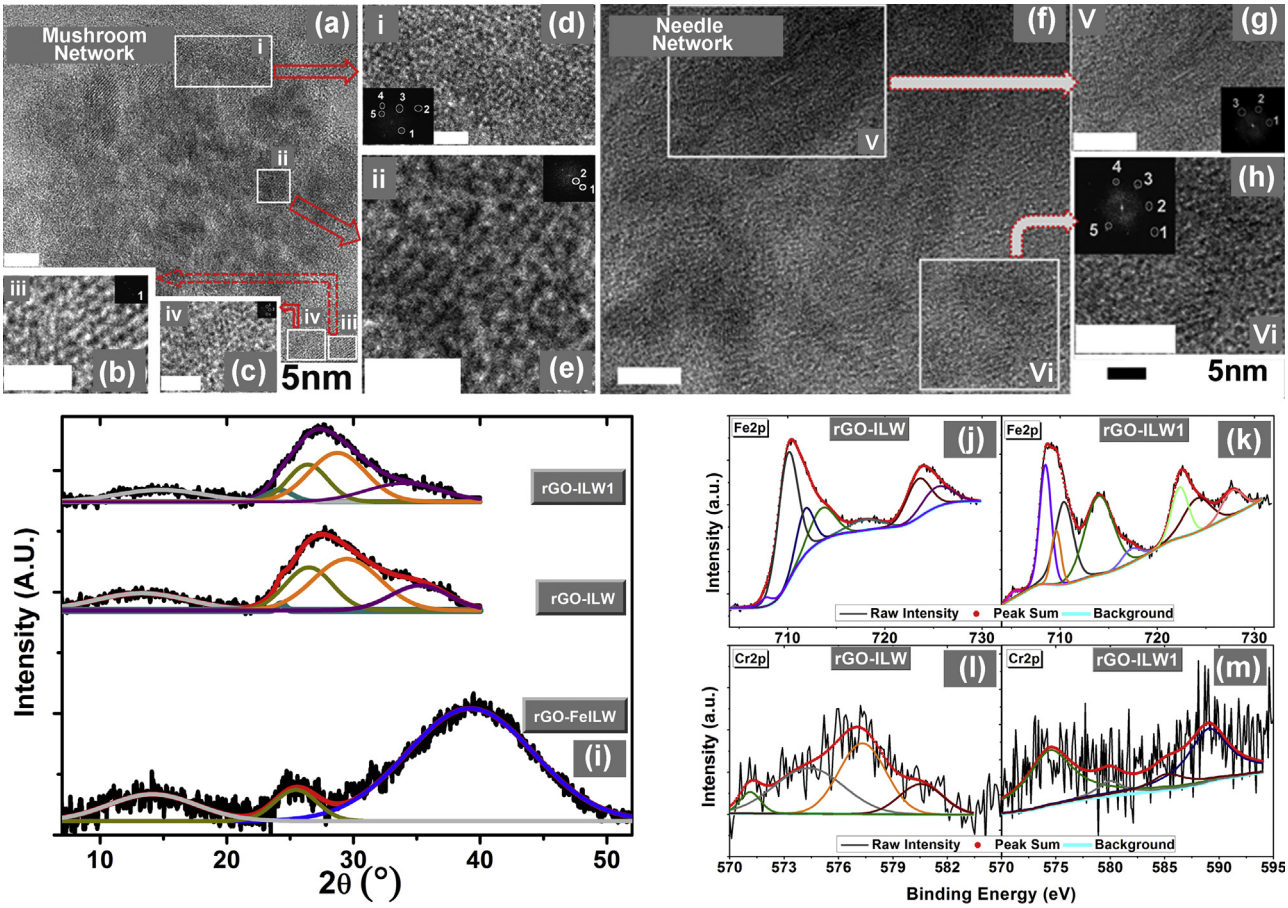

Fig. 5. Morphological and surface characterization of rGO-ILW (sediment) and rGO-ILW1 (supernatant) after chromium sorption.
HRTEM images of rGO-ILW showing (a) mushroom network of nanodiscs tilted with each other (b–e) lattice images taken from different nanodiscs confirming the WAXS results indicated by the FFT pattern shown in the inset for each lattice of image (b) iii, (c) iv, (d) i and (e) ii (f) nano needle network with lattice images (IIb, c) indicating slight increase in the interlayer spacing (i) comparative de convoluted WAXS patterns of rGO-FeILW before and after sorption. The Fe2p core level spectra of the sediment and supernatant of (j) rGO-ILW and (k) rGO-ILW1 hybrid materials after hexavalent Cr sorption (summary of their respective parameters summarized in Table S5). Comparative deconvoluted Cr2p core level spectra of (l) rGO-ILW (89% Cr^{3+}) and Cr-graphene organometallic compound with $CrCl_3$ as the major component (m) rGO-ILW1Cr^{3+} (61.3%) and a Cr-graphene organometallic compound.

plexations in the graphitic matrix could explain the significantly enhanced removal efficiency of functionalized rGO over its unfunctionlised form and chromium entrapment resulting in $[(C_6H_6)_2Cr]$. In such a system, Cr^{6+} reduction to Cr^{3+}/Cr^0 could occur *via* a charge transfer mechanism. To investigate this possibility, XPS was employed.

Variation and peak position in the UV spectra showed almost 100% sorption was achievable with the absorbing material and notably higher than the value obtained by ICP-MS for rGO-FeILW (data not shown). The difference may arise from the interference of organic matter in the samples or limitations in detecting organic-Cr complex by ICP-MS. Structural and microstructural details of samples before and after Cr sorption were monitored by WAXS analysis using deconvoluted patterns owing to the broadness of the peak and fitted to a Gaussian function. Microstructural variation before (rGO–FeIL) and after Cr sorption was observed by examining both the sediment (rGO–IL) and supernatant (rGO–IL1) obtained after centrifugation (Table S6).

After exposure of rGO–FeIL to chromium and washing (rGO–FeILW), distinct morphological structures evident from the microstructural patterns pertaining to floral mushroom-like regions (Fig. 3a) surrounded by needles (Fig. 4a, c and d) of relatively weak contrast composed of 2–5 nm particle aggregates are observed that most likely exist as hydrogen-bonded porous networks formed from the alkyl chain of IL. These are clearly visible in Fig. 4d. Further in contrast to rGO-FeIL, continuous lattice fringes (Fig. 4b) of the encircled region of Fig. 4a are representative of larger sheets of rGO or modified rGO of interlayer spacing of the order ca 0.13, 0.21 and 0.25 nm. The morphological appearance of needles may in fact originate from the site of the mushroom structures *via* water/IL assisted fragmentation of the sheets. The lattice images observed from the two different morphologies of rGO–ILW are shown in Fig. 5(a–h). A closer examination of the fringe pattern in the mushroom structure (Fig. 5a) shows the continuous network to be composed of small pockets of fringes possibly comprising nanodiscs that are tilted with respect to neighboring nanodiscs. The interlayer spacing from the FFT of selected regions (0.37 nm, 0.35 nm) shown within the square borders (Fig. 5a, squares i–iv) (Fig. 5(b–e)) is in accordance with WAXS observation (Fig. 5i). Further the HRTEM image and respective FFT of nanoneedles network is shown in Fig. 5(f–h). It is noted that the interlayer spacing in the nano needles are slightly larger than the reference materials of 0.23/0.25 nm (Fig. 5g) and 0.26 nm (Fig. 5h) but smaller than the nanodiscs within the mushroom networks indicating washing of unbound foreign species.

The comparison of interplaner spacing (Table S6) shows slight increase in rGO-IL along 0 0 1 indicative of defects originating from the removal of unbound IL. Rationalizing changes in ionic radii of Cr^{3+} (61.5 pm) and Cr^{6+} (44 pm), occurrence of incremental differences in interlayer spacing strongly suggests entrapment of Cr

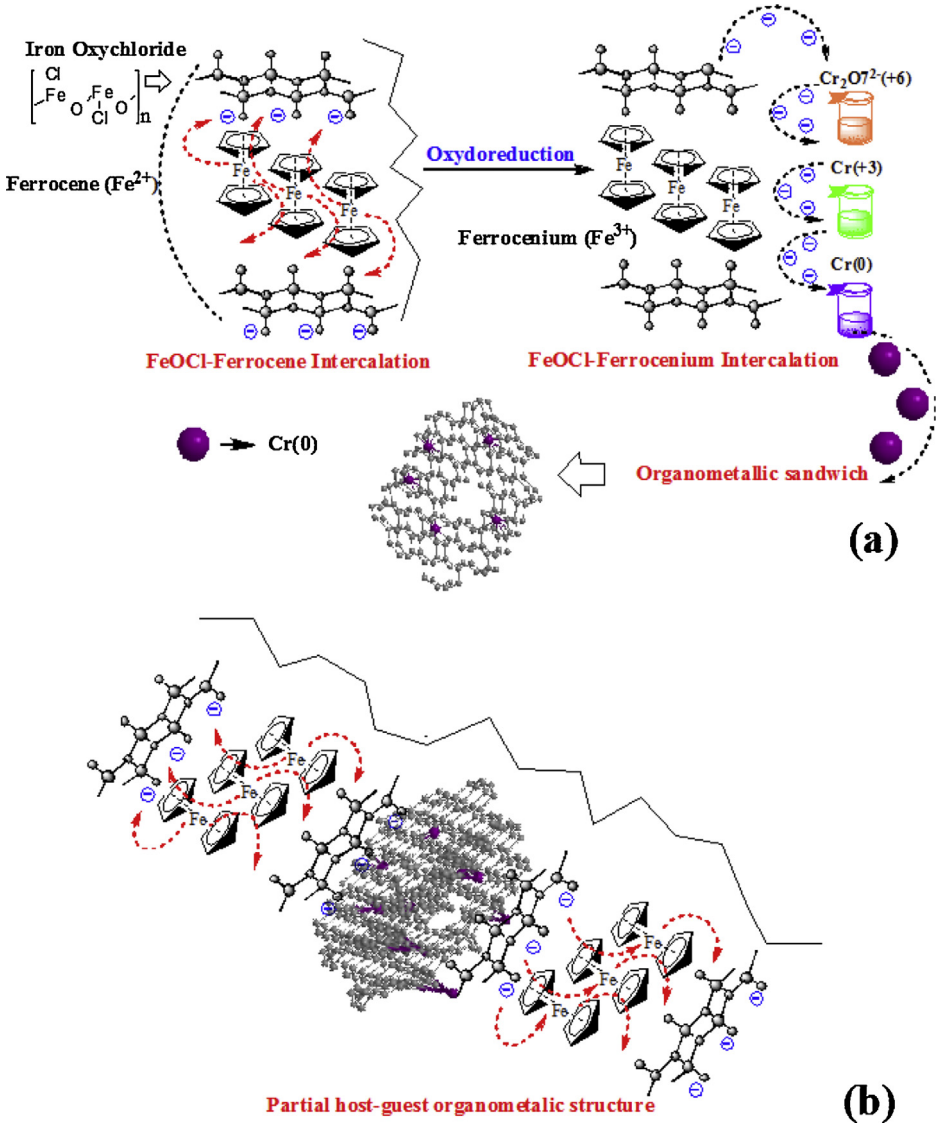

Fig. 6. Proposed mechanism of chromium sorption by rGO-FeIL.
(a) Formation of organometallic complex of reduced native Cr between the layers of graphene mediated by host guest structure *via* oxydo-reduction and (b) the overview of the final structure.

ions descending from oxidation +6 to +3. Notably, binding energies from core-level Cr2p spectra (Fig. 4h and i) obtained for both the sediment and supernatant material fractions exposed to different chromium environments; Cr^{3+} and Cr^{6+} discernible by the presence of $HCrO_2$, (Cr^{3+}, Cr2p3/2) at 577 eV, Cr_2O_3 at 586.5 eV along with $K_2Cr_2O_7$ (Cr^{6+}, Cr2p1/2) at 588.7 eV. The presence of Cr_2O_3 and $K_2Cr_2O_7$ was later confirmed from O1s BEs at 530.4 eV and 531.8 eV as shown in Fig. S6. In addition to Cr_2O_3 and $K_2Cr_2O_7$, the presence of CrN at 572.3 eV and Cr–C at 584.1 eV signifies a definitive interaction between the IL environment and the nanohybrid material in the supernatant. rGO–FeILW showed strong association with Cr^0 sandwiched between the ring structures of graphene from the presence of the predicted organometallic type structure [$(C_6H_6)_2Cr$] evidenced by the Cr2p and C1s BE peak at 574.1 eV and 284.5 eV respectively. The existence of Cr^{3+} and Cr^{6+} in the form of $HCrO_2$ at 577 and CrO_3 at 580.4 eV respectively also signified variability in the oxidation state of Cr (Fig. 5l, m and Table S7).

The effect of Cr interaction on behavioral properties of Fe are shown in the narrow region of Fe2p spectra (Fig. 5f–h, k). The Fe2p spectra of sediment (rGO–IL) and supernatant (rGO–IL1) of the pure reaction after Cr sorption indicates the presence of FeOCl, FeO, $FeCl_3$ and ferrocenyl moieties. However, the Fe2p spectra of the water washed sediment of the washed catalyst (rGO–ILW) shows only 11.6% ferrocenyl moieties together with a substantially larger amount of ferrocenium (42%) and FeOCl (27.5%). The supernatant of the water washed catalyst (rGO–ILW1) showed an elevation in the content of ferrocenyl moieties to 17.2% compared to the sediment fraction and oxide variants of Fe and the Fe chloride complex, $FeCl_3$ (Table S8). Further, the absence of ferrocenium and FeOCl is a key feature of this spectra suggesting a strong association of the ironoxy chloride to the ferrocenium complex of the graphitic structure. As mentioned, the consistency of the observed d-spacing 0.81, 0.39 and 0.34 nm in close approximity to the interplaner spacing of (0 1 0), (1 0 0) and (0 0 1) of FeOCl and the probable intercalation of the ironoxy chloride with the organometallic ferrocene is further substantiated by Cl2p core spectra (Fig. S3) indicating the consumption of free Cl ions (19.9%) and loss of $FeCl_4^-$ (53.8%) before water hydrolysis leading to the generation of FeOCl (28.8%) and appearance of C—Cl bonds (31.8%) after water hydrolysis. The significance of the geometrical intercalation of FeOCl at defect sites supports its role as a guest molecule in the reduction of Fe from ferrocenium

to ferrocene. This is correlated to the reduction of Fe^{3+} following to Fe^{2+} following electron transfer from Fe^{3+} to chromium ions and hence the catalytic cycle.

The presence of Cr sandwiched between the ring structure of graphene in form of an organometallic type structure $[(C_6H_6)_2Cr]$ is a probable route to stabilize Cr^0 from the Cr2p (Fig. 5l, m, Table S7). Hence, the nanocatalytic properties of ferrocene effectively reduce Cr^{6+} evidenced by the increase in oxidation state of Fe from 2+ to 3+ supporting its role in oxydoreduction of entrapped chromium in $[(C_6H_6)_2Cr]$. It is worth emphasizing that the ratio $(Cr^{3+} + Cr^0)/Cr^{6+}$ is higher in water washed samples and maximum in rGO–ILW indicating that mesoporous graphene is ideally suited for hexavalent Cr removal among the hybrid materials. The generation of the ironoxy chloride FeOCl mentioned above is substantially depleted (Table S8) after chromium sorption and the reduced peak indicates that it may participate in the electron charge transfer process facilitating the role of the ferrocene–graphene redox nanocatalyst.

In the present work, it is evident that the removal of hexavalent Cr in its recyclable form is mediated by reductive sorption of Cr in a multi-step process as opposed to a simple reduction event. Here, we propose a novel mechanism of oxidative reduction in which the maximum removal of Cr (VI) is achieved by combining a host guest chemical mechanism with the organometallic complex formation (Fig. 6). Here, the FeOCl host structure is formed in the presence of rGO–FeILW. It has been reported however, that the release of FeOCl is affected by the presence of glycerol through stabilization of FeOOH. The stabilization of FeOCl suggests that the reduction rate of GO exceeds the formation of FeOOH and favors stabilization of FeOCl. Formation of FeOCl, a layered metastable structure of Fe reportedly occurs *via* the interaction of Fe_2O_3 with $FeCl_3$. Hence, FeOCl can be exploited as a host material that takes advantage of van der waals layers between chlorine–chlorine stacking. This also provides a reactive interface for open edges in rGO–ILW to associate with Cl from FeOCl. The occurrence of a simultaneous reaction involving the modification of the released cation that forms a ferrocene type ion by the interaction of $FeCl_2$ in the presence of potassium occurs favorably resulting in a ferrocene type 'sandwich' structure. In the second step, the host guest chemistry plays an important role. FeOCl is a well-known host material for organic based compounds and thus we propose that the attachment or localisation of FeOCl to graphene defect sites hosts the modified IL to form a supramolecular cage-type structure. Further, the ability of the FeOCl host to provide OH^- as an electron donor group from its role as an efficient catalyst [41] aids the oxidation of the guest molecule conversion from ferrocene to ferrocenium. This is evidenced by XPS indicating the presence of ferrocene and ferrocenium in rGO-ILW. The release of electrons from the subsequent loss of OH^- from FeOCl and conversion of ferric to its ferrous state leads to the reduction of hexavalent Cr to Cr^0 (Fig. 6). Further, the reduced Cr^0 interacts with the sp^3 carbons forming a sandwich-like entrapment composed of $[(C_6H_6)_2Cr]$ (Fig. 6) as evidenced by WAXS, HRTEM and XPS. We propose that a synergetic electron transfer process assisted by the host catalyst and guest ferrocene forming caged structures efficiently reduces hexavalent Cr.

Acknowledgment

This work was supported by the National Research Foundation of Korea (NRF) grant funded by Korea government (MEST) (No. NRF-2010-0029227, NRF-2012R1A1A2008196, NRF-2012R1A2A2A01047189). Dr. V. Khare gratefully acknowledges financial support from BK21 program of the government of Korea.

Appendix A. Supplementary data

Supplementary data associated with this article can be found, in the online version, at http://dx.doi.org/10.1016/j.apcatb.2015.09.008.

References

[1] H. Hu, J.H. Xin, H. Hu, X. Wang, D. Miao, Y. Liu, J. Mater. Chem. A (2015).
[2] A.R. Ribeiro, O.C. Nunes, M.F.R. Pereira, A.M.T. Silva, Environ. Int. 75 (2015) 33–51.
[3] L. Järup, Br. Med. Bull. 68 (2003) 167–182.
[4] F. Bernardis, R. Grant, D.C. Sherrington, React. Funct. Polym. 65 (2005) 205–217.
[5] J. Granatier, P. Lazar, R. Prucek, K. Šafářová, R. Zbořil, M. Otyepka, P. Hobza, J. Phys. Chem. C 116 (2012) 14151–14162.
[6] L. Fan, Q. Zhang, K. Wang, F. Li, L. Niu, J. Mater. Chem. 22 (2012) 6165–6170.
[7] M.B. Avinash, K.S. Subrahmanyam, Y. Sundarayya, T. Govindaraju, Nanoscale 2 (2010) 1762–1766.
[8] Y. Gao, G. Hu, W. Zhang, D. Ma, X. Bao, Dalton Trans. 40 (2011) 4542–4547.
[9] K. Deng, J. Zhou, X. Li, Electrochim. Acta 95 (2013) 18–23.
[10] Y. Lu, Y. Jiang, H. Wu, W. Chen, Electrochim. Acta 156 (2015) 267–273.
[11] F. Zapata, A. Caballero, A. Espinosa, A. Tárraga, P. Molina, J. Org. Chem. 74 (2009) 4787–4796.
[12] G. Kalita, S. Sharma, K. Wakita, M. Umeno, Y. Hayashi, M. Tanemura, Phys. Chem.Chem. Phys. 15 (2013) 1271–1274.
[13] Z. Zhang, C.H. Turner, J. Phys. Chem. C 118 (2014) 24633–24640.
[14] P. Wasserscheid, W. Keim, Angew. Chem. Int. Ed. 39 (2000) 3772–3789.
[15] C.C. Brasse, U. Englert, A. Salzer, H. Waffenschmidt, P. Wasserscheid, Organometallics 19 (2000) 3818–3823.
[16] P.F. Fulvio, P.C. Hillesheim, J.C. Bauer, S.M. Mahurin, S. Dai, J. Mater. Chem. A 1 (2013) 59–62.
[17] V. Khare, Z. Li, A. Mantion, A.A. Ayi, S. Sonkaria, A. Voelkl, A.F. Thunemann, A. Taubert, J. Mater. Chem. 20 (2010) 1332–1339.
[18] R.E. Morris, Chem. Comm. (2009) 2990–2998.
[19] S. Some, Y. Kim, Y. Yoon, H. Yoo, S. Lee, Y. Park, H. Lee, Sci. Rep. 3 (2013).
[20] V. Khare, M.-Q. Pham, N. Kumari, H.-S. Yoon, C.-S. Kim, J.-I.L. Park, S.-H. Ahn, ACS Appl. Mater. Interfaces 5 (2013) 4063–4075.
[21] A. Wolfson, C. Dlugy, Y. Shotland, Environ. Chem. Lett. 5 (2007) 67–71.
[22] Y. Gu, J. Barrault, F. Jérôme, Adv. Synth. Catal. 350 (2008) 2007–2012.
[23] A. Díaz-Álvarez, V. Cadierno, Appl. Sci. 3 (2013) 55–69.
[24] Zhao Qina, Markus Buehlera, Mol. Simul. 38 (2012) 695–703.
[25] R. Gobel, Z.-L. Xie, M. Neumann, C. Gunter, R. Lobbicke, S. Kubo, M.-M. Titirici, C. Giordano, A. Taubert, CrystEngComm 14 (2012) 4946–4951.
[26] H.S.S. Ramakrishna Matte, K.S. Subrahmanyam, K. Venkata Rao, S.J. George, C.N.R. Rao, Chem. Phys. Lett. 506 (2011) 260–264.
[27] S. Baldelli, J. Bao, W. Wu, S.-s. Pei, Chem. Phys. Lett. 516 (2011) 171–173.
[28] P.L. de Andres, R. Ramírez, J.A. Vergés, Phys. Rev. B (2008) 1–10.
[29] Y. Si, E.T. Samulski, Chem. Mater. 20 (2008) 6792–6797.
[30] Y. Song, X. Kang, N.B. Zuckerman, B. Phebus, J.P. Konopelski, S. Chen, Nanoscale 3 (2011) 1984–1989.
[31] G. Zou, W. Hu, D. Taguchi, T. Manaka, M. Iwamoto, Chem. Commun. 49 (2013) 8105–8107.
[32] J. Kotakoski, A.V. Krasheninnikov, U. Kaiser, J.C. Meyer, Phys. Rev. Lett. 106 (2011) 105505.
[33] M. Batzill, Surf. Sci. Rep. 67 (2012) 83–115.
[34] Kristine D. Butcher, Stephen V. Didziulis, Bernard Briat, E.I. Solomon, J. Am. Chem. Soc. 112 (1990) 2231–2242.
[35] I. de Pedro, A. Garcia-Saiz, J. Gonzalez, I. Ruiz de Larramendi, T. Rojo, C.A.M. Afonso, S.P. Simeonov, J.C. Waerenborgh, J.A. Blanco, B. Ramajo, J.R. Fernandez, Phys. Chem.Chem. Phys. 15 (2013) 12724–12733.
[36] B.S.V. Ivády, V. Zólyomi, A. Gällström, N.T. Son, E. Janzén, A. Gali, Mater. Sci. Forum 717–720 (May) (2012) 205–210.
[37] O. Cretu, A.V. Krasheninnikov, J.A. Rodríguez-Manzo, L. Sun, R.M. Nieminen, F. Banhart, Phys. Rev. Lett. 105 (2010) 196102.
[38] P.M. Morris, J.D. Brown, Z. Naturforschg 20b (1965) 597.
[39] J.A. Labinger, Inorg. Chim. Acta 424 (2015) 14–19.
[40] J.C. Green, M.L.H. Green, G. Parkin, Chem. Commun. 48 (2012) 11481–11503.
[41] X.-j. Yang, X.-m. Xu, J. Xu, Y.-f. Han, J. Am. Chem. Soc. 135 (2013) 16058–16061.
[42] Y.S. Sohn, D.N. Hendrickson, J. Hart Smith, H.B. Gray, Chem. Phys. Lett. 6 (1970) 499–501.
[43] M.S. Goldsztaub, Bull. Soc. Fr. Minéral. Crystallogr. 58 (1935), 6–76.S.
[44] A. Pekker, M. Chen, E. Bekyarova, R.C. Haddon, Mater. Horiz. 2 (2015) 81–85.
[45] L. Leita, A. Margon, A. Pastrello, I. Arčon, M. Contin, D. Mosetti, Environ. Pollut. 157 (2009) 1862–1866.
[46] G.A. Domrachev, S.Y. Ketkov, G.A. Razuvaev, J. Organomet. Chem. 328 (1987) 341–348.
[47] J.H. Osborne, W.C. Trogler, P.D. Morand, C.G. Francis, Organometallics 6 (1987) 94–100.
[48] Y.C. Song, R.L. Hu, A.K. Soh, Phys. Scr. 2007 (2007) 136.
[49] W.L. Jolly, The Synthesis and Characterization of Inorganic Compounds, Prentice-Hall, New Jersey, 1970, pp. 484–487.